Steady state model and experiment for an oscillating grid turbulent two-layer stratified flow

Lilly Verso,[1,*] Maarten van Reeuwijk,[2] and Alex Liberzon[1]

[1]*School of Mechanical Engineering, Tel Aviv University, Tel Aviv 69978, Israel*
[2]*Department of Civil and Environmental Engineering, Imperial College, SW7 2AZ London, United Kingdom*

Turbulence generated by an oscillating grid in a two-layer stably stratified system is a classical flow utilized to study various aspects of turbulence in presence of stratification without mean shear. This flow evolves in a quasisteady state, in which the layer thickness and density difference evolves in a quasisteady manner due to the large separation of timescales between the turbulence and the setup. We present an extension of the classical setup that enables full steady state conditions and in which the entrainment velocity can be prescribed separately from the Richardson number. We develop a theoretical box-model and show that the model is in good agreement with the experiments. The model allows to predict the transient response of the system for a variety of initial conditions and the imposed steady state. The new setup is necessary to obtain the steady position of the density interface, for example, when using advanced optical techniques to measure the small-scale features of turbulence near the interface.

I. INTRODUCTION

Turbulent entrainment involves the transport of mass, momentum, and mixing of scalar quantities across an interface between a turbulent layer and a nonturbulent layer. The process is of great importance for the dynamics of the ocean [1–3], atmospheric pollution [4,5], bio-mass production [6,7], and oil-spill propagation [6,8], among other applications. One of the canonical experimental setups to study turbulent entrainment without mean shear is a stratified two-layer fluid system of different densities, in which turbulence is created in one of the layers by an oscillating grid [9,10]. The setup has been used extensively since [11–14], as reviewed by Fernando [15,16].

Turner [10] determined the entrainment velocity w_e via the time rate of change of the thickness of one of the layers. An entrainment coefficient $E = w_e/w^*$ is defined as a ratio of w_e to the typical turbulence intensity at the interface w^*. An "entrainment law" of the form $E = A\,\mathrm{Ri}^{-n}$ relates the entrainment coefficient to the the Richardson number Ri that represents the stability parameter of the density interface. The exponent $n = 3/2$ was measured for the layers of different salinity and $n = 1$ for temperature stratified layers [10]. There is, however, no full consensus on the value of n [17] for the salinity-stratified case. For instance, Xuequan and Hopfinger [18] and Wolanski *et al.* [19] confirmed the findings of Turner [10], while Fernando and Long [20,21] obtained a higher value of $n = 1.75$ in saline stratified solutions.

With the enormous advances in the field of optical measurement techniques, such as three-dimensional particle tracking velocimetry (3D-PTV) [22,23], it has become possible to study entrainment in unprecedented detail. However, optical setups take a long time to set up and are difficult to calibrate, making it important to be able to control where the turbulent-nonturbulent interface resides. In the classical setup, the system evolves in a quasisteady state, and the layer thickness and density difference between the layers are slowly varying functions of time. This significantly complicates optical measurements: a moving interface that crosses the field of view during the measurement invalidates the careful calibration and hinders the measurement quality.
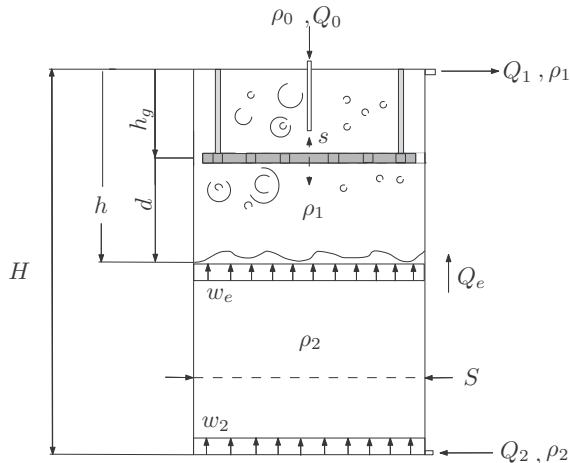
---

*lillyverso@mail.tau.ac.il

FIG. 1. Sketch of the extended two-layer stratified setup.

Furthermore, the continuously changing density, scales of turbulence, the entrainment rate, and the Richardson number, within the measurement volume make it impossible to collect significant statistics through time averaging.

Previous studies stabilized the density interface in the Turner setup by discharging fluid from the bottom of the tank at the same rate of the entrainment flux [19] or used oscillating grids in both layers. Both techniques do indeed stop the interface, but the density in the top layer is not in a steady state, implying that the system is not fully stationary. Hopfinger and Linden [24] stabilized the buoyancy flux by adding fresh water on top of the lighter layer or heating the top of the water column, thus keeping its density nearly constant, but still had a nonnegligible rate of propagation of the interface.

Thus, a system in which the steady state can be achieved, i.e., the interface is not moving and the density of the two layers remain constant over relatively long time, is needed.

In this study, we modify the classical setup such that the experimental facility allows for steady-state solutions, by adding additional controlled inflows and outflows. The paper is structured as follows. In Sec. II, we describe the new experimental setup, and we develop a simple theoretical box-model for predictive purposed in Sec. III. We describe the experiments in Sec. IV, as well as the calibration of the grid-action parameter K, which describes how efficient the grid is in producing turbulence. The laboratory experiments are compared to the model in Sec. V and it is shown that the two are in good agreement with each other. Conclusions and recommendations are made in Sec. VI.

II. THE EXPERIMENTAL SETUP

The starting point is the classical Turner setup [10], which comprises a fluid layer of uniform density ρ_1 on top of a layer of density $\rho_2 > \rho_1$, thus creating a stable stratification (Fig. 1). Turbulence is introduced by a vertically oscillating horizontally oriented grid located at depth h_g in the top layer, which oscillates at fixed frequency f and at a stroke length s. The novel feature of the experiment presented here is two additional pumps that supply volumetric flow rates Q_2 and Q_0, with heavy fluid at density ρ_2 to the bottom layer, and light fluid to the top layer at density ρ_0, respectively. The inflows cause an overflow from the top at a rate $Q_1 = Q_0 + Q_2$ and density ρ_1, such that the overall volume of fluid in the tank remains constant. Due to interaction of the grid turbulence with the density interface, fluid of density ρ_2 is entrained and mixed into the top layer. The net flux of volume that crosses the interface is quantified by the entrainment flux Q_e.

The thickness of the top layer and the distance of the grid to the free surface are denoted as $h(t)$ and h_g, respectively. Both quantities are measured from the free-surface water level. The distance of the interface to the grid middle-position is indicated with d and the total height of the tank is denoted H. In the sketch, we introduced the inlet velocities $w_0 = Q_0/S$ and $w_2 = Q_2/S$, the outlet velocity $w_1 = Q_1/S$ and the entrainment velocity $w_e = Q_e/S$, where S is the horizontal cross-sectional area of the tank.

When the pumps are switched off, the system is a replica of the Turner setup [10]. In this case, continuous turbulent agitation induces propagation of the density interface at a rate $\frac{dh}{dt} \neq 0$ and mixing of heavy fluid into the top layer implying that $\frac{d\rho_1}{dt} \neq 0$, and thus the setup is not in a steady state. When the pumps are switched on, the bottom pump counteracts the interface propagation due to the turbulence, while the top pump refreshes the fluid in the top mixed layer. When the grid starts from rest, the top layer either grows or shrinks as a result of the turbulent agitation and inflows until it reaches the steady-state condition, where the interface propagation is arrested and the density difference $\Delta\rho$ between the two layers remains constant.

III. THE MODEL

In the following, we present a predictive model of the steady state of the system in terms of the position of the interface $h(t)$, the buoyancy of layers $b_1(t)$, and the overall Richardson number Ri.

The turbulence generated by an oscillating grid in an unstratified medium is typically described using the model of Long [25], which relates the turbulent intensity and length scales to the distance from the planar grid. The root mean square of the horizontal fluctuations u_{rms} and the integral length scale L are parameterized as [25,26]

$$u_{\text{rms}} = Kd^{-1}, \tag{1}$$

$$L = \beta d, \tag{2}$$

where K is the so-called "grid action" parameter and β is an empirical constant, depending on the grid frequency, stroke length, and mesh size [21,24]. Based on these two quantities, a Reynolds number can be defined as

$$\text{Re} = \frac{u_{\text{rms}}L}{\nu} = \frac{K\beta}{\nu}, \tag{3}$$

where ν is the viscosity of the turbulent layer. Note that Re is independent of the distance to the grid, implying that the turbulence has a uniform value of Re throughout the turbulent layer. The buoyancy is defined by using ρ_2 as the reference density:

$$b = g\frac{\rho_2 - \rho}{\rho_2}, \tag{4}$$

which implies that the buoyancy in the bottom layer b_2 is zero by definition. The bulk Richardson number is representative of the strength of the stratification relative to the turbulence levels near the interface inside the turbulent layer and it is defined as

$$\text{Ri} = \frac{L^*(b_1 - b_2)}{u_{\text{rms}}^{*2}} = \frac{\beta\, d\, b_1}{K^2}, \tag{5}$$

where $(*)$ indicates quantities calculated at the interface location.

In the classical mixing box setup, Turner [10] observed an entrainment relation of the form

$$E = w_e/u_{\text{rms}}^* = A\,\text{Ri}^{-n}, \tag{6}$$

where A and n are coefficients. For the salinity-based stratification, values of $A = 3.8$ and $n = -1.5$ were reported [10,26].

The model assumes that the two layers remain well mixed throughout the experiment and are separated by an infinitesimally thin interface. Furthermore, it is assumed that the Boussinesq approximation is applicable. Under these assumptions, volume and buoyancy conservation in the top layer are given by

$$\frac{dh}{dt} = w_e - w_2, \tag{7}$$

$$\frac{d(b_1 h)}{dt} = w_0 b_0 - (w_0 + w_2) b_1. \tag{8}$$

Substituting Eqs. (1) and (6) into the steady-state solution of the system described in Eqs. (7) and (8), we arrive at the steady-state description in terms of the entrainment velocity, buoyancy, and distance of the interface from the grid:

$$w_e^s = w_2, \tag{9}$$

$$b_1^s = \frac{w_0}{w_0 + w_2} b_0, \tag{10}$$

$$d^s = \left(\frac{K^{1+2n}}{w_2 b_0^n} \frac{A}{\beta^n} \right)^{\frac{1}{1+3n}} \left(\frac{w_0 + w_2}{w_0} \right)^{\frac{n}{1+3n}}, \tag{11}$$

where we add superscript $()^s$ to denote the steady-state solution. When the steady state is reached, w_e^s is an imposed quantity, which depends only on the inflow velocity w_2. This implies that the entrainment flux Q_e^s can be prescribed and controlled by the bottom pump flow rate Q_2.

A. Dimensionless equations

We normalize the system by scaling the equations using the steady-state conditions

$$t = \frac{d^s}{w_2} \hat{t}, \quad h = d^s \hat{h}, \quad b = b_1^s \hat{b}_1, \quad d = d^s \hat{d}, \tag{12}$$

which results in

$$\frac{d\hat{d}}{d\hat{t}} = \hat{w}_e - 1, \tag{13}$$

$$\hat{h} \frac{d\hat{b}_1}{d\hat{t}} = \frac{w_0}{w_2} \hat{b}_0 - \frac{w_0}{w_2} \hat{b}_1 - \hat{w}_e \hat{b}_1, \tag{14}$$

where $\hat{w}_e = \frac{w_e}{w_2} = \hat{d}^{-1-3n} \hat{b}_1^{-n}$. By introducing the flux ratio ϕ and the dimensionless distance between the grid and the free surface $\hat{h}_g$, defined as

$$\phi = \frac{w_0 + w_2}{w_2}, \quad \hat{h}_g = \frac{h_g}{d^s}, \tag{15}$$

Eq. (14) can be rewritten as

$$(\hat{d} + \hat{h}_g) \frac{d\hat{b}_1}{d\hat{t}} = \phi(1 - \hat{b}_1) - (\hat{w}_e - 1)\hat{b}_1. \tag{16}$$

Equation (16) demonstrates that, for a fixed position of the interface, the steady state exists only when the two terms of the right-hand side are equal. Therefore, to achieve the steady state, the flux ratio ϕ must be finite and assume values different from zero.

Shown in Fig. 2 are phase space trajectories for four different initial conditions at $\hat{h}_g = 1$ and $\phi = 0.1, 1.0, 5.0,$ and 10.0, which are roughly representative for the experiments what will be presented in the next section. As expected, all solutions converge to the fixed point for which $\hat{b}_1 = 1$
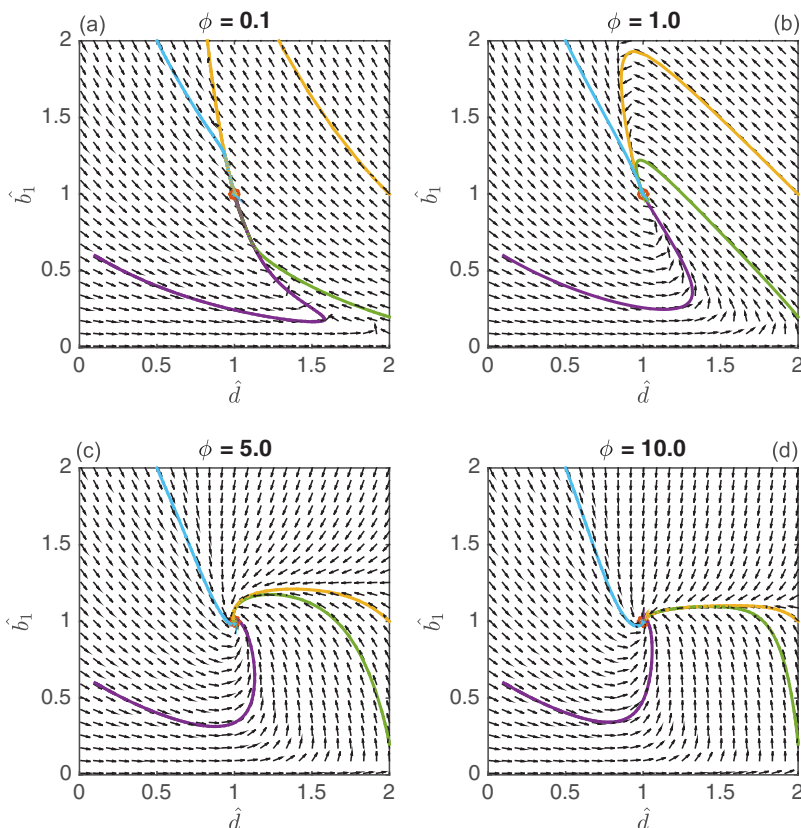
FIG. 2. Typical phase trajectories for the system Eqs. (13) and (16) for $\hat{h}_g = 1$, and (a) $\phi = 0.1$, (b) $\phi = 1.0$, (c) $\phi = 5.0$, (d) $\phi = 10.0$.

and $\hat{d} = 1$. As can be seen in the phase trajectories, the solutions need not converge uniformly to the fixed point, overshoots in $\hat{d}$ and $\hat{b}_1$ are the norm rather than the exception.

There are two dominant time scales in this system. The first is the timescale of the experimental setup $\tau_R \sim d/w_e$, which represents the time required to replenish all the fluid beneath the grid. The second time scale is related to the mixing time scale of turbulence at the interface, τ_L. The flow integral time scale was estimated using auto-correlations of $u'(x)$ that provide the integral length scale of the flow L, followed by $\tau_L = L/u^*_{\mathrm{rms}}$. The time scale to reach the steady state τ_R is typically much larger than a typical time scale of the turbulence τ_L. Indeed, in the experiments introduced in the next section, the time scales can be estimated as $\tau_L = [1.4 \div 2.1]$ s and $\tau_R = [1.1 \div 6.7]$ h for different combinations of controlling parameters. The separation of time scales is such that the system will evolve in a quasisteady state as far as the turbulence and turbulent entrainment is concerned.

IV. EXPERIMENTS AND TECHNIQUES

We performed seven different experiments, enumerated as 1–7, in a glass tank with a $200 \times 200\ \mathrm{mm}^2$ cross-section and a depth of 300 mm shown in Fig. 1. At the initial time $t = 0$ the stratification is made by carefully placing a fresh water layer of density $\rho_0 = \rho_1(t = 0)$ upon a saline-water solution of density ρ_2. The experimental parameters are summarized in Table I.

We carried out most of the experiments (2–7) in a combination of fresh water and Epsom salts ($MgSO_4$) with different concentrations, focusing on the key mechanisms for the steady state in the system. In addition, we run case 1 in an index-matched conditions [27]. This combination reduces

TABLE I. Experimental parameters: initial and final density differences, inflow rates, initial and steady-state Richardson and Reynolds numbers, controlling parameters, and uncertainty levels.

| Case | $\Delta\rho$ [kg/m^3] | | Q_0 | Q_2 | Ri | | Re | | ϕ | $\hat{h}_g$ | $\varepsilon_{\hat{d}}$ | $\varepsilon_{\hat{b}}$ |
	t_0	t_f	[ml/min]	[ml/min]	Ri_0	Ri^s	Re_0	Re^s			[%]	[%]
1	14	18	40	40	43	100	18 470	26 635	2	0.78	1.8	12.5
2	54	25	40	40	153	88	25 352	21 471	2	0.91	2.8	6.3
3	50	26	40	40	70	104	25 352	21 471	2	0.91	2.8	6.5
4	55	38	0	0	50	360	24 291	23 642	∞	—	—	—
5	101	79	0	0	120	340	24 636	22 149	∞	—	—	—
6	129	91	0	0	133	518	22 418	18 457	∞	—	—	—
7	102	119	87	6.5	536	327	19 865	23 911	14.4	0.96	2.5	0.9

major limitations of optical velocity measurements across the interface such as a distortion of the laser sheet and of the scattered light to the camera [28]. However, brilliant techniques have been developed to match the refractive index of two solutions with different densities [29,30]. To avoid double diffusivity phenomena and guarantee the largest possible density ratio between the two fluids, for case 1 the best combination results in a lighter solution of ethanol and water and a heavier saline solution of Epsom salts and water.

The initial and final values of the density jump $\Delta\rho$, Ri and Re are presented, respectively, in Table I, along with the inlet volumetric fluxes of the upper pump Q_0 and the bottom pump Q_2, the dimensionless controlling parameters of ϕ and $\hat{h}_g$, and the uncertainty between the model and the experiment, at the steady state. The uncertainty is quantified through the relative error $\varepsilon_x = |x - x_0|/x \times 100\%$, where x and x_0 are the theoretical prediction and experimental observation, respectively, for a quantity marked in the subscript, for the normalised depth $\varepsilon_{\hat{d}}$ and buoyancy $\varepsilon_{\hat{b}}$.

In experiments 4, 5, and 6 we study the fully transient behavior of the classical mixing box setup, and the two inflow pumps were switched off. For experiments 1, 2, 3, and 7 we use pumps to obtain different values of the control parameter ϕ.

Note that cases 6 and 7 are the two stages of the same physical experiment, performed with a long time break between them. During the first stage (case 6), we let the system evolve without pumps, and in the second stage (case 7) we switch the pumps on to achieve the steady state. In this way, we are able to probe the E-Ri law in the conditions impossible in the classical setup, when the Richardson number decreases. A similar "inverse" experiment is presented in the case 2.

Our turbulence source is an oscillating grid located in a fixed position, $h_g = 65$ mm from the free surface level. The grid size is 190 mm^2 constructed of plastic square bars of 5 mm and a mesh size $M = 25$ mm, giving a solidity of 38%. The oscillations are provided by a linear motor with an encoder of 0.01 mm positioning resolution (LinMot Hs01-37x166-GF). The stroke length s is 20 mm and the oscillation frequency is fixed at $f = 4$ Hz in all the tests.

We measure the thickness of the top layer relative to the free surface level, $h(t)$ with an accuracy of $\delta h = \pm 0.5$ mm, and density $\rho_1(t)$ in the upper layer in time with $\delta\rho = \pm 1$ kg/m^3. In the refractive index unmatched cases, the depth of the top layer $h(t)$ is measured by using a digital camera (Optronis CL4000CXP, 2304 × 1720 pixels). We used backlighting to obtain the projection of the interface shadow in the camera visualization plane. Then the horizontal average position of the vertical change in gray-scale intensity provided the measure of the interface location in respect to the free surface level. The density is measured by using a HI-8733 conductivity probe located in a corner of the tank. The device was calibrated and opportunely corrected for the case 1 (ethanol-water mixture). In this specific case, extracted samples from the outlet of the mixed solution using a small volume pycnometer of $V_p = 10$ ml with an accuracy of ± 0.01 g/ml support the probe density measurements.

To calibrate the predictive model, the quantities K, β, the two constants that depend only on the grid properties are estimated using particle image velocimetry technique (PIV) measurements. PIV was performed on the flow of the case 1. We measure two components of the velocity field in a vertical
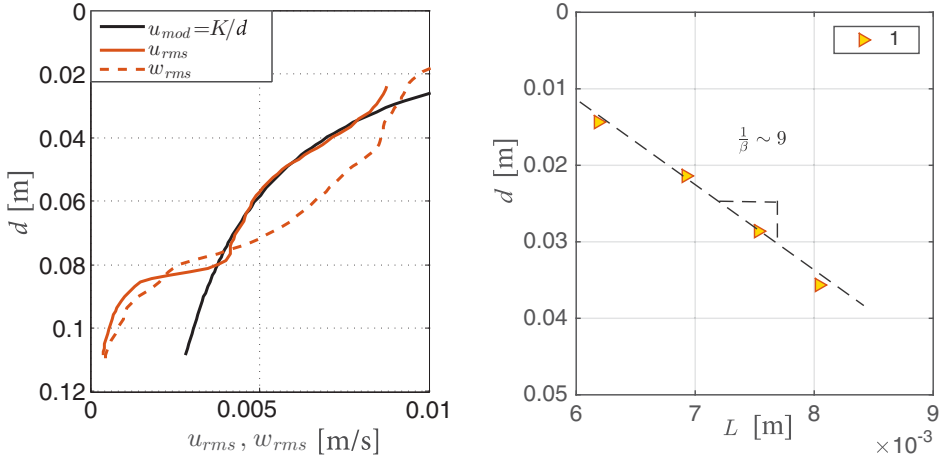
FIG. 3. (left) Spatial distibution of u_{rms} and w_{rms} and (right) the longitudinal integral length scale for the horizontal velocity component as a function of the distance from the grid d ($d = 0$ is the grid middle position). The dashed line corresponds to the linear relation $L = \beta d$. The parameters are estimated as $K = 3.2 \times 10^{-4}\,[\mathrm{m}^2/\mathrm{s}]$ and $\beta = 0.11$.

plane. The PIV system consists of a dual-head Nd:YAG laser (120 mJ, 15 Hz, NewWave Inc.) and 11 megapixel CCD camera (TSI Inc., 12 bit, 56.2 μm/pixel magnification ratio in the given setup) and the OpenPIV open source software [31] was used for the image analysis. The analysis was performed with interrogation windows of 32×32 pixels and 50% overlap. Spurious vectors were identified first by a global and a local median filters. The rejected vectors were replaced by interpolation using the local mean and the data are smoothed using a Gaussian filter. PIV measurements were performed such that particles have an average displacement of approximately 5 pixels/Δt, which corresponds to a time interval $\Delta t = 25$ ms, four times smaller than the Kolmogorov time scale, estimated as $\tau_\mu \sim 100$ ms. The velocity fields were measured in sets of 200 realizations with the acquisition frequency of 0.5 Hz at time instants of $t_1 = 1.47, 3.17, 4, 4.30$ h. This acquisition frequency is chosen to ensure that subsequent velocity measurements are uncorrelated.

The ensemble-averaged velocity fields (computed as an average of 200 instantaneous velocity fields) are denoted by angular brackets $\langle \cdot \rangle$ and the turbulent fluctuations fields are denoted as $u' = u - \langle u \rangle$ and $w' = w - \langle w \rangle$. The spatial distributions of root mean square of turbulent velocitie components are shown in the left panel of Fig. 3, as profiles obtained by additional averaging in horizontal, homogeneous direction. In this plot we present also the fit to the model of the turbulent velocity distribution $\propto d^{-1}$. The grid action parameter, K [25], is obtained from the best fit from the data.

The longitudinal integral scale L of the horizontal velocity was obtained directly from the PIV velocity measurements, by computing the auto-correlation function of the fluctuating u' at fixed distance from the grid,

$$R^{uu}(r,d) = \frac{\overline{u'(x,d)u'(x+r,d)}}{\overline{u'^2}}, \tag{17}$$

and by calculating the integral of $R^{uu}(r,d)$ to the first zero crossing. This procedure was repeated at various distances from the grid. The plot of $L(d)$ allows for fitting of β as shown on the right panel of Fig. 3. We measured $K = 3.2 \times 10^{-4}\,[\mathrm{m}^2/\mathrm{s}]$ and $\beta = 0.11$, for the turbulent flow in case 1. These values are within the range reported in previous studies [21,24].
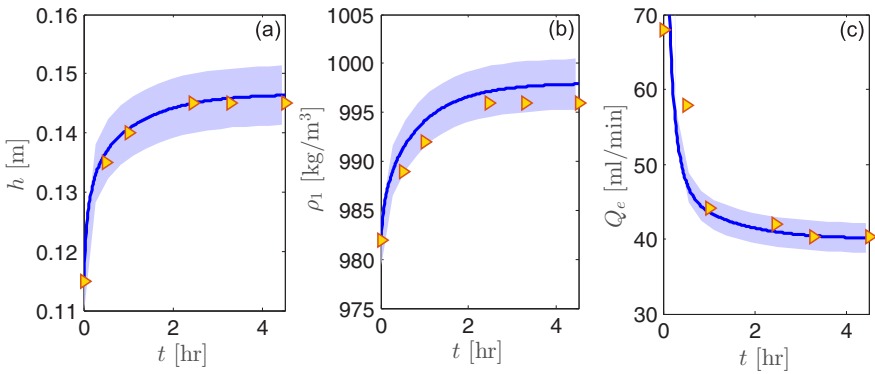
FIG. 4. Overlap of the numerical simulation (solid curves) and measured quantities (symbols) for case 1. (a) Thickness of the top layer h. (b) Density ρ_1 of the top layer. (c) Entrainment flux Q_e. The shaded regions define the uncertainty range of the experimental quantities measured.

V. RESULTS AND DISCUSSION

First, we compare the measurement results to the model predictions. Figure 4 presents and example of time evolution of $h(t)$, the density of the top layer ρ_1, and the entrainment flux Q_e for case 1. After a transient period, the steady state is visible in the experiment (symbols), in agreement with the theoretical predictions (solid curves) within the range of measurement uncertainty (shaded regions). The agreement is seen in regards to the values and the time scales of the experimental system.

Note that case 1 was performed in index-matched conditions, thus the interface between the two layers was not visible or optically detectable. In the index-matched case the interface is defined at the point of the maximum $\partial u_{\mathrm{rms}}(z)/\partial z$ based on PIV measurements of $u_{\mathrm{rms}}(z)$.

Let us briefly explain the system behavior in this and similar experimental cases. The experiment starts with the interface set close to the grid (2 mesh sizes). Due to vicinity to the oscillating grid turbulence source, the interface is perturbed by the flow, causing rapid downward motion of the interface [Fig. 4(a)]. We observe entrainment in the form of filaments that are dragged into the
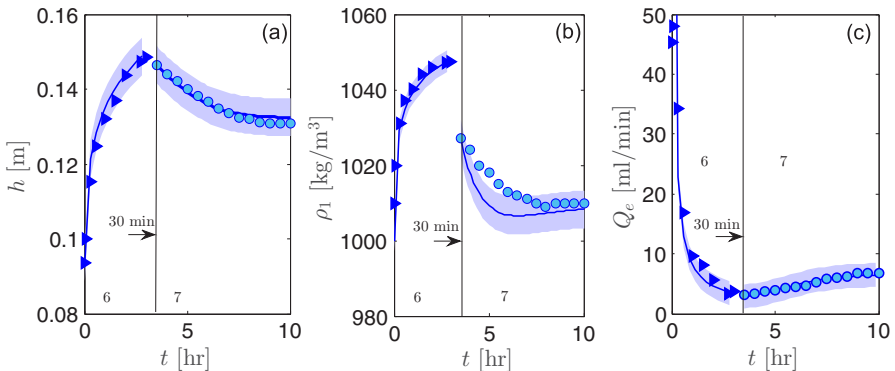

FIG. 5. Overlap of the numerical simulation and measured quantities for cases 6 and 7. (a) Thickness of the top layers h (blue triangles and cyan circle markers) with prediction (continuous line). (b) Density ρ_1 (blue triangles and cyan circle markers) and prediction (continuous line). (c) Entrainment flux Q_e (blue triangles and cyan circle markers) and prediction. The bounded region delimits the sensitivity range of the experimental quantities measured. Note, the first measurement point for case 7 is taken after 30 min of the pumps activation.
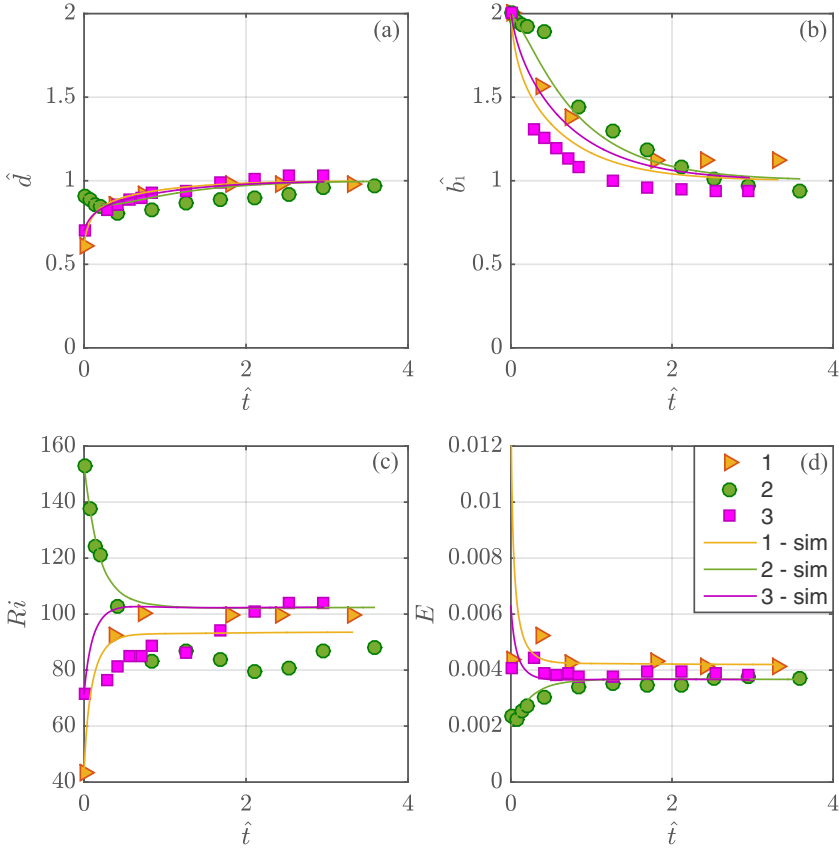
FIG. 6. Dimensionless plots of (a) depth of the mixed layer $\hat{d}$, (b) top layer buoyancy $\hat{b}_1$, (c) bulk of Richardson number Ri, and (d) entrainment coefficient E. Overlap of experimental results (markers) and simulations (continuous lines) for the steady-state cases 1, 2, and 3.

upper layer, which are quickly mixed into the turbulent top layer. The upper layer grows as shown in Fig. 4(a) and its density increases; see Fig. 4(b).

As the interface moves downward, less turbulent kinetic energy is available at the interface position. Consequently, the entrainment velocity w_e reduces, and according to Eq. (8), when the u^*_{rms} becomes comparable to the the inflow velocity w_2, the rate of propagation of the interface decreases drastically. Eventually the system settles into a steady-state situation and all the parameters, h, ρ_1, and Q_e, are constant.

In Fig. 4(c), the measurements of entrainment flux Q_e are presented. The reviewed studies estimated the quasisteady buoyancy flux Q_e based only on the velocity of the propagating interface, dh/dt [10,19,32]. Through the transient periods, uncertainty in the measurements of dh/dt and $d\rho/dt$ propagates into the estimates of Q_e. On contrary, for the steady state, $Q_e^s = Q_2$, where Q_2 is a well-controlled value. This is one of the key points in this work. Figure 4(c) shows that the flux measurements are well within the uncertainty region, extending ± 2 ml/min, which is equivalent to a maximum error of the entrainment coefficient to be $\Delta_E \approx 10^{-5}$.

In Fig. 5 we present the results of cases 6 and 7 in a similar manner. These two cases are the two different stages of the same experiment. In the case 6, the pumps are not active and the system evolves in absence of forcing flow rates. The case is fully transient, therefore the mixing layer h, the density ρ_1, and the entrainment flux Q_e change continuously for the entire duration of the test. These cases also allow for testing the validity of the theoretical model at extreme conditions: the
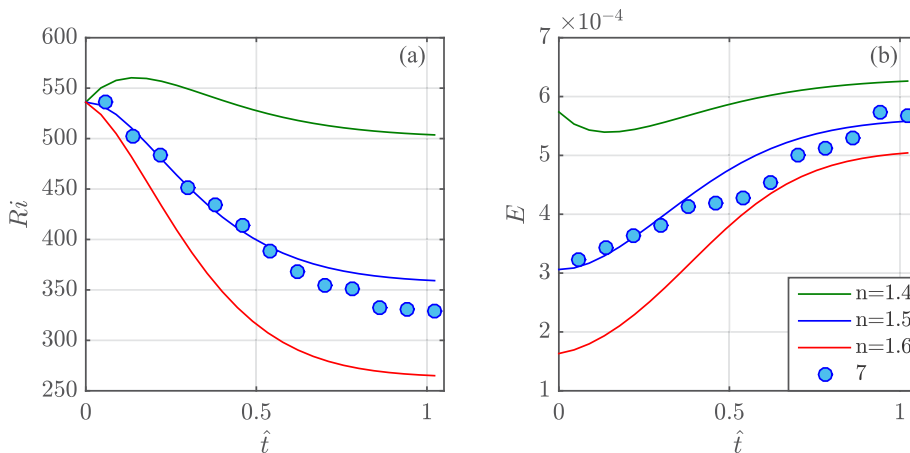
FIG. 7. (a) Richardson number and (b) entrainment coefficient predictions, obtained by repeating the predictive model for different values of the exponents n (continue lines). The simulations are overlapped to the experimental data for case 7.

saline solution in the bottom layer is close to saturation values and there is a very high initially density jump $\Delta\rho$ (see Table I).

After 3 h of case 6 test, we turned on the two pumps and initiated case 7, starting from the final conditions of case 6. The first measurement point of the second stage (case 7), was taken after 30 min from the pump activation. In this test we pushed the experimental system to a very high flux ratio $\phi = 14.4$ case (compared to $\phi = 2$ for other cases). Furthermore, this is a test case in which the initial position of the interface is about 1.5 mesh sizes below its steady-state position and not above it as in other cases. This experiment demonstrates that we can reverse the direction of propagation of the interface from a typical downwards direction to the upward motion. It is also noteworthy that in this case the interface moves toward the grid and the values of $u^*_{\rm rms}$ increase. It leads to decreasing Richardson number and increasing values of entrainment coefficient. Therefore, the developed two-layer system enables more careful exploration of the entrainment law, as we can test also the law from low to high values of entrainment rate, or from high to low values of Richardson.

In Fig. 6 the analytical model is compared with the experiments in the dimensionless form. The results of the steady-state cases are reported (1, 2, 3) together, collapsing them according to the steady-state dimensionless parameters, $\hat{d}, \hat{b}_1$ versus dimensionless time $\hat{t}$ in Figs. 6(a) and 6(b). As can be discerned from Fig. 2, the experiments are in reasonably good agreement with the predictions. Also shown in Figs. 6(c) and 6(d) are the Richardson number and entrainment rate Figs. 6(c) and 6(d), which is also shown to be in reasonable agreement with the theoretical predictions. Moreover, the test cases of different fluids are successfully compared, both refractive index matched (case 1) and unmatched cases (cases 2 and 3). This is of special importance for our future studies in which we aim to perform 3D-PTV Lagrangian measurements of particles crossing the density interface in which it is crucial to have refractive index matched solutions, but the repetitive calibration runs are prohibitively expensive.

Many studies have argued on the value of the exponent n of the entrainment relation in the two-layer case [17]. Figures 7(a) and 7(b) display the time evolutions of the Ri and E for case 7, showing the sensitivity of the model in the transient period and also supporting the value of $n = 1.5$ measured by Turner [10] and Hopfinger *et al.* [18]. The overlap of the numerical simulations and the experimental results provides an alternative way to estimate n in the transient stage. It is important to note that the experimental data of case 7 (markers) in both Ri and E series are calculated through direct measurement of the quantities b_1, h and their time derivatives dh/dt and db_1/dt. Therefore,
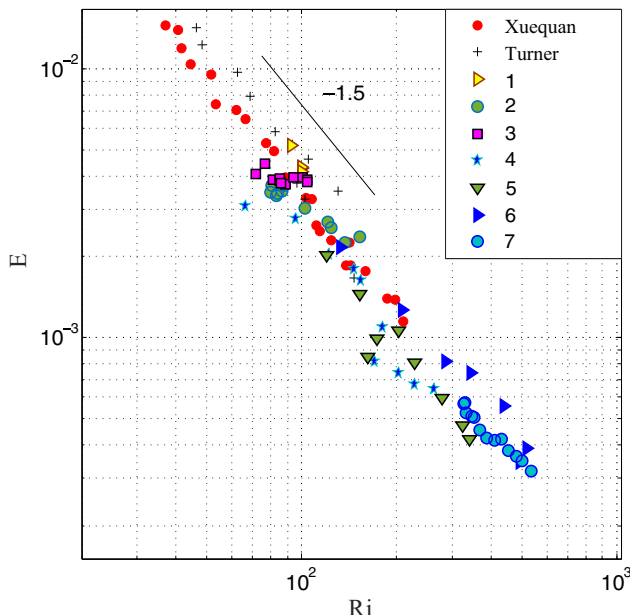
FIG. 8. The entrainment law. Overlap of cases 1–7 with previous experiments of Turner [10] and Xuequan and Hopfinger [18].

during the experiment, the Ri and E are measured independently. The experimental data are following the theoretical prediction by matching the law through the transient confirming the robustness of the model. Figure 7 shows also that the entrainment relation can be interpreted as a consequential cascade of quasisteady states of the system, naturally from low Ri and high E to high Ri and low E values. For the first time we reversed this process on the entrainment law. This is confirmed by the decreasing Richardson and increasing entrainment coefficient values in the transient period.

Figure 8 summarizes all the experimental tests on the Ri-E plot, compared to the data from the Turner [10] and Hopfinger [18] experiments. Consistent with the observed good agreement between the experiments and the theoretical predictions, the experimental results follow the slope of -1.5 similarly to the classical results in saline solutions. We plot our measurements as points in time through the transient regime to the steady state of various tests.

It is noteworthy that the experiments presented here extend the previous measurements on the E-Ri law to a broader range of Ri and E values. Moreover, the accumulation of the measurements points for the runs 1, 2, 3, and 7 during the steady state demonstrate that also the steady state of the system complies with the entrainment law. What is more important is that our system enables, to the best of our knowledge, for the first time, using the controlling parameters ϕ and $\hat{h}_g$, to set the rate of entrainment and/or the Richardson number, independently. There is also an additional noteworthy information in this figure. There are no adjustable parameters, and the results of Hopfinger and Turner [10,18] overlap the results in our setup. Furthermore, a power-law fit of all the cases provides the two additional calibration constants $A = 3.8$ and $n = 1.5$, which turns out to be universal for all the experiments in this setup (for both increasing and, as we reveal in our case, decreasing Ri).

VI. CONCLUSIONS

This paper focused on the steady state of a two-layer stably stratified flow under an oscillating grid. A modified version of the classical Turner setup [10] was proposed, with the aim to achieve the complete steady-state conditions. The modification consists of a conversion of the Turner's setup

into a closed-loop control system, by supplying fluids at constant flow rates to the tank at predefined densities and maintaining the volume constant through the outlet of the tank. In this way, the interface can be maintained at a fixed distance from the grid and maintain constant density ratio between the two layers.

We performed a theoretical and numerical analysis to study the transient behavior of the new setup. For this purpose, a theoretical box model was developed. Our analysis highlights the dependence of steady state on two dimensionless quantities, namely the flux ratio ϕ and the normalized distance from the grid $\hat{h}_g$. The model was validated by performing seven experiments in which a large range of initial conditions was tested, including one case in which the two layers were index matched. The index-matched experiment was used to perform particle image velocimetry (PIV) to obtain the spatially resolved turbulent flow fields and calibrate the model parameters. The theoretical model with calibrated parameters for the given grid was shown to predict the behavior of the system reasonably accurately, starting from a transient period and up to the steady state. Finally, we showed that our experimental measurements follow the classical results obtained by Turner [10] and Xuequan and Hopfinger [18] in saline water stratification.

This setup would be crucial for future 3D-PTV measurements of particles crossing the density interface, which will require the high-quality repeatability of the calibration runs in the refractive index matched cases that use expensive solutions. The next step of the work will be to perform extensive Lagrangian investigations to shed light on the dominant entrainment mechanism in stratified fluids. Moreover, the understanding of the basic mechanisms of steady state of the two-layer system is important for modeling and experimental purposes that attempt to characterize the steady-state entrainment laws.

[1] G. T. Csanady, Turbulent diffusion in a stratified fluid, J. Atmos. Sci. **21**, 439 (1964).

[2] A. S. Thorpe, *The Turbulent Ocean* (Cambridge University Press, Cambridge, 2005).

[3] H. J. S. Fernando, *Handbook of Environmental Fluid Dynamics* (CRC Press, Boca Raton, FL, 2013), Vol. 2013.

[4] A. G. M. Driedonks and H. Tennekes, Entrainment effects in the well-mixed atmospheric boundary layer, Bound-Lay. Meteorol. **30**, 75 (1984).

[5] M. Davidson and M. Vilhena, *Air Pollution and Turbulence Modeling and Applications* (CRC University Press, Boca Raton, FL, 2003).

[6] J. A. Knight, C. W. Gorton, and R. J. Kovac, Oil production by entrained flow pyrolysis of biomass, Biomass **6**, 69 (1984).

[7] A. P. Dykes, M. Mulligan, and J. Wainwright, *Monitoring and Modelling Dynamic Environments*, (John Wiley and Sons, New York, 2015).

[8] T. Beer, *Environmental Oceanography* (CRC University Press, Boca Raton, FL, 1995).

[9] H. Rouse and J. Dodu, Turbulent diffusion across a density discontinuity, Houille Blanche **10**, 530 (1955).

[10] J. S. Turner, The influence of molecular diffusivity on turbulent entrainment across a density interface, J. Fluid Mech. **33**, 639 (1968).

[11] I. A. Hannoun, H. J. S. Fernando, and E. J. List, Turbulence structure near a sharp density interface, J. Fluid Mech. **189**, 189 (1988).

[12] E. L. G. Kit, E. J. Strang, and H. J. S. Fernando, Measurement of turbulence near shear-free density interfaces, J. Fluid Mech. **334**, 293 (1997).

[13] D. A. Briggs, J. H. Ferziger, J. H. Koseff, and S. G. Monismith, Turbulent mixing in a shear-free stably stratified two-layer fluid, J. Fluid Mech. **354**, 175 (1998).

[14] A. Venaille, L. Gostiaux, and J. Sommeria, A statistical mechanics approach to mixing in stratified fluids, J. Fluid Mech. **810**, 554 (2017).

[15] H. J. S. Fernando, Turbulent mixing across density interfaces: A review of laboratory experiments and their oceanographic implications, in *Proceedings of the Aha Hulikoa 5th Hawaiian Winter Workshop* (1989), pp. 205–218.

[16] H. J. S. Fernando, Turbulent mixing in stratified fluid, Ann. Rev. Fluid Mech. **23**, 455 (1991).

[17] R. I. Nokes, On the entrainment rate across a density interface, J. Fluid Mech. **188**, 185 (1988).

[18] E. Xuequan and E. J. Hopfinger, On mixing across an interface in stably stratified fluid, J. Fluid Mech. **166**, 227 (1986).

[19] E. J. Wolanski and L. M. Brush, Turbulent entrainment across stable density step structures, Tellus **27**, 259 (1975).

[20] H. J. S. Fernando and R. R. Long, The growth of a grid-generated mixed layer in a two-fluid system, J. Fluid Mech. **133**, 377 (1983).

[21] H. J. S. Fernando and R. R. Long, Experiments on steady buoyancy transfer through turbulent fluid layers separated by density interfaces, Dynam. Atmos. Oceans **12**, 233 (1988).

[22] D. Krug, M. Holzner, B. Lüthi, M. Wolf, A. Tsinober, and W. Kinzelbach, A combined scanning PTV/LIF technique to simultaneously measure the full velocity gradient tensor and the 3D density field, Meas. Sci. Tech. **25**, 065301 (2014).

[23] M. Holzner, A. Liberzon, N. Nikitin, B. Lüthi, W. Kinzelbach, and A. Tsinober, A Lagrangian investigation of the small-scale features of turbulent entrainment through particle tracking and direct numerical simulation, J. Fluid Mech. **598**, 465 (2008).

[24] E. J. Hopfinger and P. F. Linden, Formation of thermoclines in zero-mean-shear turbulence subjected to a stabilizing buoyancy force, J. Fluid Mech. **114**, 157 (1982).

[25] R. R. Long, Theory of turbulence in a homogeneous fluid induced by an oscillating grid, Phys. Fluids **21**, 1887 (1978).

[26] E. J. Hopfinger and J. A. Toly, Spatially decaying turbulence and its relation to mixing across density interfaces, J. Fluid Mech. **78**, 155 (1976).

[27] T. J. McDougall, On the elimination of refractive-index variations in turbulent density-stratified liquid flows, J. Fluid Mech. **93**, 83 (1979).

[28] A. Alahyari and E. K. Longmire, Particle image velocimetry in a variable density flow: Application to a dynamically evolving microburst, Exp. Fluids **17**, 434 (1994).

[29] M. Economidou and G. R. Hunt, Density stratified environments: the double-tank method, Exp. Fluids **46**, 453 (2009).

[30] G. Oster and M. Yamamoto, Density gradient techniques, Chem. Rev. **63**, 257 (1963).

[31] Z. J. Taylor, R. Gurka, G. A. Kopp, and A. Liberzon, Long-duration time-resolved piv to study unsteady aerodynamics, IEEE T. Instrum. Meas. **59**, 3262 (2010).

[32] L. H. Kantha and R. R. Long, Turbulent mixing with stabilizing surface buoyancy flux, Phys. Fluids **23**, 2142 (1980).